Towards safe shearography inspection of thick composites with controlled surface temperature heating

Tao, Nan; Anisimov, Andrei G.; Groves, Roger M.

DOI
10.1016/j.ndteint.2023.102907

Publication date
2023

Document Version
Final published version

Published in
NDT and E International

NDT&E International 139 (2023) 102907

Contents lists available at ScienceDirect

NDT and E International

journal homepage: www.elsevier.com/locate/ndteint

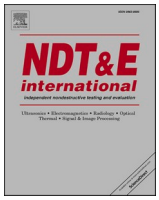

Towards safe shearography inspection of thick composites with controlled surface temperature heating

Nan Tao *, Andrei G. Anisimov, Roger M. Groves

Department of Aerospace Structures and Materials, Faculty of Aerospace Engineering, Delft University of Technology, Kluyverweg 1, 2629 HS, Delft, the Netherlands

ARTICLE INFO

Keywords:
Thick composites
Shearography
Controlled surface temperature heating
Deep defect detection
FEM

ABSTRACT

Thick glass fiber-reinforced polymer (GFRP) composites, e.g. thickness of more than 50 mm, are increasingly used in a wide variety of industries, particularly in the marine and wind energy sectors. Defect detection and characterisation in these composites remain appealing challenges due to the material complexity and the presence of various manufacturing and in-service defects. In this study, we propose a novel shearography method with controlled surface temperature (CST) heating for deep defect detection (i.e., 15 mm depth and more) in thick GFRP laminates. The proposed CST heating has been developed based on analytical solutions to control the maximum surface temperature of a test object during shearography inspection. Numerical and experimental studies have been performed to analyse the defect behaviour and defect detection under various heating scenarios, a topic which is rarely reported for thick composites with shearography. Compared with conventional shearography, the CST shearography method maximises heating energy input with a controlled and stable maximum surface temperature for deep defect detection. Results indicate an enhancement of about 27% in defect signal for the defect at 15 mm depth in comparison to conventional heating. The results also provide insight for implementing an efficient inspection in terms of the inspection duration and the number of datasets. This study makes a step towards safe, quantitative and predictable inspection of deep defects in thick composites.

1. Introduction

Benefiting from the improvement of advanced manufacturing techniques, thick composite materials [1–3], represented by glass fiber-reinforced polymer (GFRP) and carbon fiber-reinforced polymer (CFRP), are increasingly being adopted in various industries including marine [1,4], aerospace [5,6] and wind energy [7,8]. For example in the marine RAMSSES project [9], a real-scale (6 m in height and 2.5 m in width) full composite hull section was manufactured from fiber-reinforced solid laminates and sandwich structures. The thickness of the hull varied in the range 50–300 mm. Thick composite materials have superior advantages of weight-reduction and corrosion resistance over traditional metallic materials [1,2,5]. Therefore, they offer a significant contribution to reducing fuel consumption and greenhouse gas emissions. These materials tend to be used in safety-critical applications such as large primary or secondary load-bearing structures, where a structural failure may cause catastrophic consequences [2,10,11]. Hence inspection of thick composite materials is urgent for both informing the maintenance and repair processes and for further advancing thick composite structure performance. However, defect detection and characterisation in thick composites (especially for deep defects) remain an appealing problem due to their significant thicknesses, material complexity, and the presence of various defects [10,11].

Although many non-destructive testing (NDT) techniques have been adopted for defect detection in composite materials such as ultrasonic testing [1,5], thermography [12,13], vibration analysis [14,15] and X-ray [16,17], they may have problems when inspecting thick composites. For example for ultrasonic testing, it can be time-consuming to scan an entire structure such as a ship hull. Besides, the attenuation of ultrasound signals and practical issues with high surface roughness of the test object can be significant [10,11]. For thermography, it is difficult to heat evenly a large structure and to avoid rapid heat dissipation. Therefore the ability to detect deeply buried defects is limited [10,11]. Among the various NDT methods available, digital shearography [18,19] is an optical interferometry method that has proven to be promising for thick composite inspection [1,20]. It offers remarkable advantages [21–23] including full-field and non-contact measurement, and the capability of detecting various defects (e.g. delamination, fiber

* Corresponding author.
E-mail address: n.tao@tudelft.nl (N. Tao).

https://doi.org/10.1016/j.ndteint.2023.102907
Received 5 April 2023; Received in revised form 21 June 2023; Accepted 5 July 2023
Available online 7 July 2023

breakage, and impact damage). Shearography is used to characterise surface strain components (i.e. displacement derivatives) under loading, allowing it to identify defect-induced strain anomalies. Loading methods commonly used in shearography include thermal, vacuum, pressure, and vibration [19,21]. Common loading methods may have difficulties when inspecting thick composites. For example for vacuum loading [21], a vacuum test chamber is required and total enclosure is usually not practical for large and thick structures. Internal pressurization [21] is suitable for pipes, pressure vessels and honeycomb structures, but it may not be suitable for thick solid laminate plates. As for vibration, a PZT or shaker is often needed for dynamic excitation; it can be challenging for thick composites due to high stiffness. In this work, thermal loading was used because of its advantages [23–25] of being non-contact, versatile and convenient for on-site inspection.

Common heating methods in shearography include flash, step, and lock-in heatings [26–28]. The combination of the lock-in method and Fourier transformation achieved an improved signal-to-noise ratio in defect imaging [29]. Later multi-frequency lock-in heating [30] was applied, which showed the capability of obtaining defect depth information with less computational time. More recently, frequency-modulated photothermal excitation has been utilized in shearography and depth-tomographic profiles of subsurface structure can be generated [31]. To sum up, the aforementioned studies have made significant contributions to developing shearography inspection, increasing its readiness level, and allowing efficient inspection of composite materials. However, these studies were limited to thin materials (less than 10 mm thickness) and shallow defects. Little research work has been done for defect detection, particularly deep defect detection (e.g., defect depth at 15 mm or more) in thick composites of 50 mm thickness and more.

One concerning issue related to shearography with thermal loading is that thermal damage may occur if the maximum surface temperature exceeds a safe level, e.g. 80 °C for the material of the introduced composite hull section in the RAMSSES project [9]. In conventional shearography methods such as flash shearography, high energy pulses can lead to over 100 °C for a fraction of a second, which may irreversibly damage a test object [26]. While in the cases of thick composites and deep defects, the shearography signal with a normal excitation level is usually low. To increase the signal, the heating can be increased and can reach kW power for minutes and dozens of minutes. This heating amount may be dangerous. Hence the maximum surface temperature of the test object needs to be controlled and thus a new modulated heating is needed for safe shearography inspection. The focus needs to be placed on controlling the maximum surface temperature, meanwhile, the heating needs to be applied in an efficient way to save inspection time. To the best of our knowledge, no literature has reported on a modulated heating method that enables the control and selection of maximum surface temperature for thick composite inspection.

Our previous work combined the finite element method (FEM) with shearography to study the defect detection capability of shearography in thick GFRP laminates [20]. Later spatially modulated heating was developed for shearography, where a reference undamaged panel was needed to compare with a defective one [32]. Nevertheless, temporally modulated heating has not been studied yet and the influence of different heating scenarios on defect behaviour and defect detection (especially for deep defects) remains unknown.

In this work, we aim to investigate deep defect detection in thick composites with shearography. For that, a controlled surface temperature heating (CST) is proposed that enables the control and selection of the maximum surface temperature during heating. A GFRP laminate 51 mm thick with flat bottom holes was manufactured to simulate major defects in thick composites, following a standard practice [33,34]. Defect behaviour and defect detection under three heating scenarios including a new controlled surface temperature heating case and two conventional heating cases were studied by a combination of numerical modelling and experimental study. The article is organized as follows. Section 2 introduces the test GFRP specimen, shearography theory and continuous strain measurement, the principles for achieving controlled surface temperature heating and our modelling approach. Section 3 presents results and discussion. First a model validation for the transient temperature and the surface strain of the thick GFRP laminate with experimental data is given in Section 3.1. Afterward, the analysis of various heating scenarios on defect behaviour and defect detection is addressed in Section 3.2. Conclusions are given in Section 4.

2. Methodology

2.1. Specimen description

The specimen of this study is a GFRP laminate made from E-glass fiber and vinyl ester resin. The layup of the composite laminate is $[0/45/90/-45]_{60}$ and the dimensions of the laminate are $600 \times 450 \times 51$ mm^3 (Fig. 1(a)). To reliably simulate major defects in this laminate, thirteen flat bottom holes were manufactured with different diameters (D = 30, 60 and 120 mm). The remaining thicknesses of the holes (Z) vary from 5 to 30 mm, representing artificial defects at different depths. The selection of material and specimen, stacking sequence, defect size and depth are representative for composite ship construction [9]. The defect size of 60 mm is comparable with industrial needs. Besides, defect sizes of 30 and 120 mm were also manufactured to explore the sensitivity of the shearography technique. It can be noted that when drilling flat bottom holes, manufacturing errors exist between the designed remaining thickness values and the actual ones. Experimentally measured thickness values (in brackets in Fig. 1(a)) were used for the FEM model in Section 2.4. The artificial defects are labelled using design values for convenience. The thermal and mechanical properties of the composite laminate (e.g., thermal expansion coefficients, specific heat, elastic modulus) that were used for modelling can be found in Ref. [20].

To understand the material and structural complexity of the GFRP specimen, X-ray micro-CT scans were performed for small samples (about $25 \times 20 \times 51$ mm^3) cut from the same GFRP laminate material. Fig. 1(b) shows a 3D reconstruction CT scan (spatial resolution: 25 μm) of a small sample and its internal stitched structure. A few manufacturing defects, e.g., voids, were found in the material. As these manufacturing defects are small (0–2 mm) compared with the artificial defects (~60 mm), they can be neglected in this study. Nevertheless, we should acknowledge that the presence of the manufacturing defects and imperfections may affect local mechanical and thermal properties, e.g., local stiffness.

In this paper we focus on defects Z15, Z20 and Z25 with a diameter of 60 mm (in orange color in Fig. 1(a)) for the objective of deep defect detection and due to a limitation of the field of view of the shearography system used (about 380×320 mm^2). The results from the three defects Z15, Z20 and Z25 will be presented in Section 3.

2.2. Shearogaphy system enabling continuous strain measurement

Shearography theory and operation principle are well documented, see for example [18,19]. A schematic of the shearography setup based on a Michelson interferometer is shown in Fig. 2. The specimen surface was illuminated by scattered laser light. The effect of the shearing device is to create a pair of identical but laterally sheared images in the CCD camera, where the neighboring points, separated by shearing distance δx, interfere with each other, creating a speckle interferogram. The optical phase φ of the speckle interferogram contains surface information of the test specimen, which can be obtained through temporal phase-shifting techniques [19]. When the test specimen is slightly deformed (e.g. by thermal loading), the corresponding speckle interferogram is slightly changed. Shearography measures surface strain components by comparing the phase difference ($\delta\varphi$) of two deformation states (φ, φ') [18,19]:

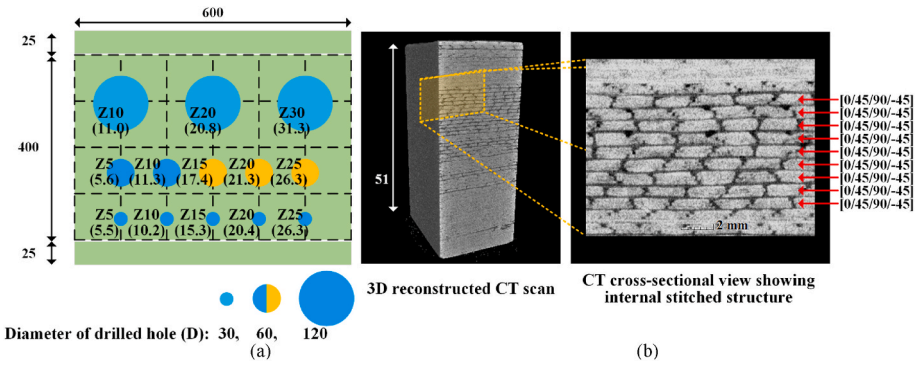

Fig. 1. (a) Diagram of the GFRP specimen with design value prefixed by Z and experimentally measured hole thickness in brackets. (b) Micro-CT scan of a small GFRP sample. The specimen and the sample were cut from the same larger GFRP panel. [Dimensions in mm].

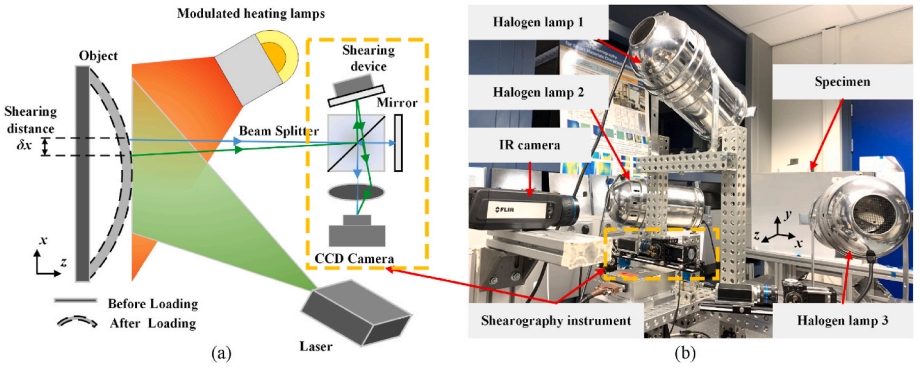

Fig. 2. Schematic of shearography (a) and the experimental system (b). The specimen is placed at a distance of approx. 1 m from the shearography instrument.

$$\delta\varphi = \varphi' - \varphi \tag{1}$$

In this paper, one channel of the previously developed 3D shape shearography instrument [35] was adopted for the investigation. The choices of the shearography camera oriented perpendicular to the specimen and the shearing direction along the x-axis (Fig. 2(b)) were made to measure the out-of-plane deformation (i.e., $\partial w/\partial x$) as the corresponding deformation is expected to be dominant for blind holes and delaminations. In this study, the selection of the x-shear direction was determined experimentally due to its efficacy in defect detection. The phase difference $\delta\varphi$ can be written as [18,19]:

$$\delta\varphi = \frac{4\pi}{\lambda}\frac{\partial w}{\partial x}\delta x \tag{2}$$

where λ is the wavelength of the laser and δx is the shearing distance in the x-direction.

Traditional shearography methods suffer from a lack of awareness of the full process of transient deformation [31] and the applied load is usually not fully characterised [32]. In the proposed shearography method with the CST thermal loading, the whole surface thermal deformation during the cooling of the specimen was continuously measured and analysed to obtain a comprehensive understanding of thick composite inspection. It should be noted that during the heating, shearography measurements were not available as the light from the lamps can saturate the shearography camera sensor.

The shearographic data processing procedure (Fig. 3) is as follows. First, the recorded sets of phase-shifted speckle interferograms were computed sequentially to generate phase differences of neighboring sets $\delta\varphi_{m-1,m}$:

$$\delta\varphi_{m-1,m} = \varphi_m - \varphi_{m-1} \tag{3}$$

By summing up the phase difference sequence, a stack of phase maps $\Phi_{0,m}$ corresponding to the reference state right after heating (t_0) was built up, representing the evolution of thermal deformation in the out-of-plane direction during the inspection:

$$\Phi_{0,m} = \sum_{i=1}^{m} \delta\varphi_{i-1,i} \tag{4}$$

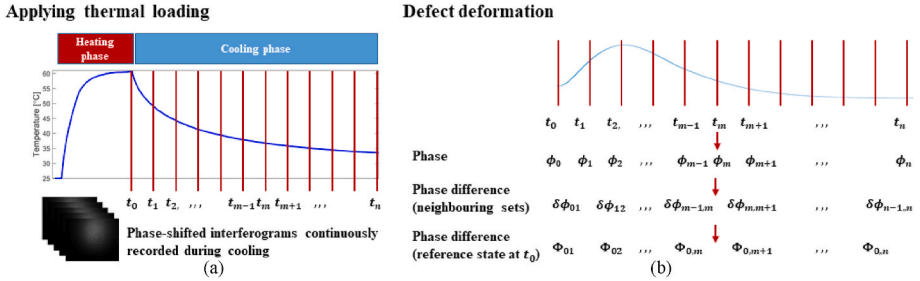

Fig. 3. Shearography with CST heating: (a) continuous measurement during cooling, (b) sequential shearographic data processing.

The efficacy of thick composite inspection with shearography may vary with different reference states [32]. The change of reference state from t_0 to t_m can be achieved by the equation below:

$$\Phi_{m,i} = \Phi_{0,i} - \Phi_{0,m} \tag{5}$$

When taking the reference state as the end of the inspection (t_n):

$$\Phi_{n,i} = \Phi_{0,i} - \Phi_{0,n} \tag{6}$$

During the experiments, three halogen lamps (Fig. 2(b)) were used for heating the specimen. The nominal electrical power of the three lamps was controlled in the range of 0–1000 W each by specific hardware. The actual heat flux from the lamps on the specimen surface with heating power was calibrated in the lab before performing the controlled surface temperature heating. The calibration was done in the full range of the lamps heating power with the surface temperature measured by the IR camera. Then the actual heat flux was calculated by solving an inverse problem from the thermal response (measured surface temperature) [20,32]. The 7th-degree polynomial was fitted in the experimental data points and further used for a direct control of the heat flux on the surface for the controlled surface temperature heating. The actual heat flux range from the lamps on the specimen surface is up to 1400 W/m^2. In this study, three heating scenarios (Fig. 4) were designed based on the idea of controlling maximum surface temperature and were applied in the shearography experiments:

(1) CST780s (solid red line): new controlled surface temperature heating method for 780 s, the maximum surface temperature increases and then remains at 60 °C during heating.
(2) CH780s (blue line): conventional constant heat flux heating with the same heating time as the CST780s case. The maximum surface temperature was the same as the CST780s case with reduced heating power.
(3) CH278s (black line): conventional constant heat flux heating with full maximum available power. The maximum surface temperature was the same as the CST780s case with a reduced heating time of 278 s.

As shown in Fig. 4, the maximum surface temperature in the CST heatings can remain around 60 °C for 20 min and more (CST1380s in dotted red line). This indicates that the proposed CST heating can control the surface temperature for a long period of heating. In other words, it allows high heating energy input with a controlled and stable maximum surface temperature for deep defect detection.

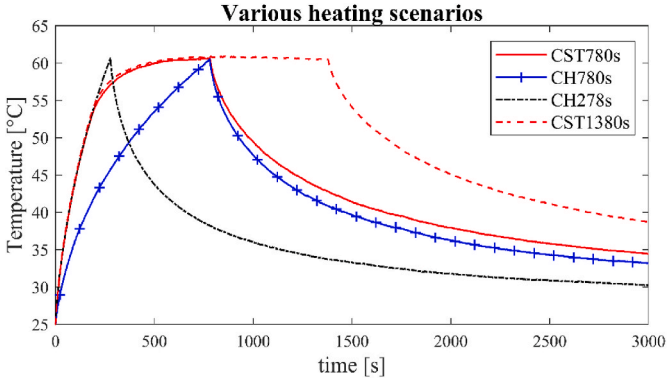

Fig. 4. Various heating scenarios used in the investigation. CST780s, CH780s and CH278s were applied in the shearography experiments; CST1380s as a reference to validate that the proposed CST heating can control the surface temperature for a long period of heating.

2.3. Controlled surface temperature heating

For thick composite inspection and deep defect detection with shearography, the defect signal with a normal thermal excitation level is usually low. To increase the defect signal, the heating intensity and time need to be significant. This heating amount may be dangerous when the surface temperature of the test object exceeds a certain value, e.g. 80 °C for the used specimen [9]. Hence the maximum surface temperature needs to be controlled for safe shearography inspection.

This section presents the principles of controlled surface temperature heating during the thermal excitation of the object. Here the problem is simplified as a 1D heat transfer problem where heat propagates in the through-thickness direction z, therefore the thermal properties of conductivity in the through-thickness direction (k_z) and the corresponding thermal diffusivity ($\alpha_z = k_z/\rho c_p$) are considered. Under the heating scenario of constant surface temperature, the surface temperature of the specimen $T(0,t)$ is controlled to be a constant value T_s over time t:

$$T(0,t) = T_s \tag{7}$$

As the specimen is thick (~51 mm) and its thermal diffusivity in the through-thickness direction is small ($\alpha_z \approx 0.23 \times 10^{-6}$ m^2/s for the used specimen [20]), the analytical solution of a semi-infinite solid [36] was applied to obtain the transient temperature of the specimen $T(z,t)$ through-thickness direction (z):

$$\frac{T(z,t) - T_s}{T_i - T_s} = \mathrm{erf}\left(\frac{z}{2\sqrt{\alpha_z t}}\right) \tag{8}$$

Where T_s is the controlled surface temperature, T_i is the initial temperature of the specimen before heating, erf is the error function, α_z is thermal diffusivity in the through-thickness direction, and t is the heating time.

So the calculated heat flux q_s on the specimen surface ($z = 0$) is [36]:

$$q_s = -k_z \left.\frac{\partial T}{\partial x}\right|_{z=0} = \frac{k_z(T_s - T_i)}{\sqrt{\pi \alpha_z t}} \tag{9}$$

Where k_z is the laminate conductivity in the through-thickness direction.

Eq. (9) shows that in order to achieve controlled constant surface temperature heating, the applied heat flux should be proportional to the reciprocal of the root of heating time t.

In this study, the initial temperature of the specimen T_i is about 25 °C and the controlled surface temperature T_s is set to 55–60 °C to obtain a safe and reasonable temperature increase for defect detection. The theoretically calculated heat flux over time is shown in Fig. 5 (black line). It can be seen that heat flux goes to infinity when heating time t is close to 0 s, so this case is not practical in experiments. As a compromise, we first heat the specimen with the full maximum available power to get the desired temperature as fast as possible (about 30 °C increase in 180

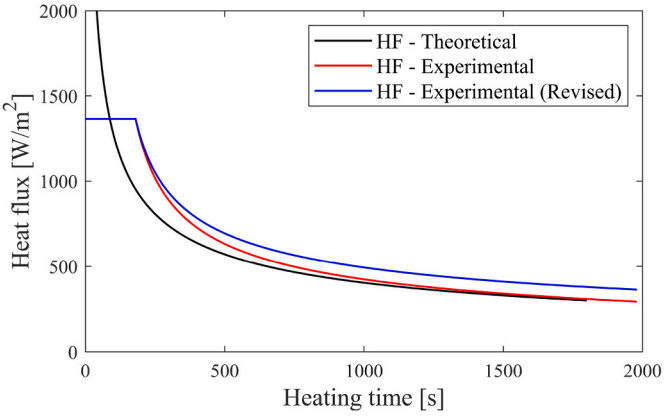

Fig. 5. Calculated heat flux for controlled surface temperature heating.

s) and then apply modulated heating following Eq. (9) to maintain a controlled constant surface temperature. The calculated heat flux is shown as the red line in Fig. 5. It should be acknowledged that Eq. (9) does not take heat loss into account. So to compensate for heat loss in experiments, we further modified the heat flux by a factor of approx. 1.1 (blue line in Fig. 5). The factor was experimentally determined for this study.

In shearography applications with thermal loading, the selection of heating time often highly depends on experience or practice, which may affect the effectiveness of the inspection. Here we determine heating time based on thermal penetration depth ($\delta_p = 2.3\sqrt{\alpha_z t}$) [36], which is related to the thermal diffusivity in the thickness direction (α_z) of the material and time t. The thermal penetration depth of the test GFRP specimen is shown in Fig. 6.

For defects at about 15, 20 and 25 mm depth (Z15, Z20, Z25) in this GFRP specimen, it takes 160–220, 290–390 and 450–610 s, respectively, for heat to propagate. Therefore, the heating time was chosen to be 180 s of full power heating plus 600 s of modulated heating, resulting in a total heating time of 780 s for the CST780s case. These should be reasonable parameters for the investigation. It is also seen that it takes 1800–2500 s for heat to propagate to the back surface of the specimen (51 mm), which is much longer than the selected heating time. So Eq. (9) is expected to be valid in the chosen heating duration. In experiments, we measured the temperature profiles of the front surface for different modulated heating times, and they show a stable constant surface temperature heating with a variation of one standard deviation of 0.64 °C from the desired 60 °C within 1380s heating (red dotted line in Fig. 4).

2.4. Modelling approach

FEM was carried out by using Abaqus CAE software. Three heating scenarios, the CST780s, CH780s, and CH278s cases (Fig. 4), were modelled. The established FEM model (Fig. 7) enables a more comprehensive understanding of various heating scenarios on defect behaviour and defect detection in thick composite with shearography.

As the test composite laminate has repeating substructures ([0/45/90/-45]), equivalent thermal and mechanical properties can be used for modelling to save computational time. There are a number of methods that can be used [37,38]. In this study, the equivalent mechanical properties were calculated with equal strain assumption according to Ref. [39] so that three-dimensional elastic properties can be obtained. The required equivalent properties including effective elastic moduli for modelling can be found in Ref. [20]. For this study, effective laminate conductivities were measured 10 times with a Hot disk TSP2200

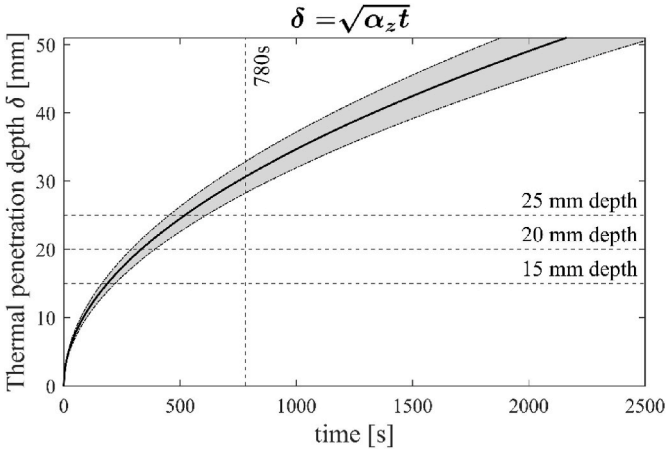

Fig. 6. Thermal penetration depth of the GFRP laminate, a 15% variation in thermal diffusivity in the through-thickness direction α_z is indicated by the grey region.

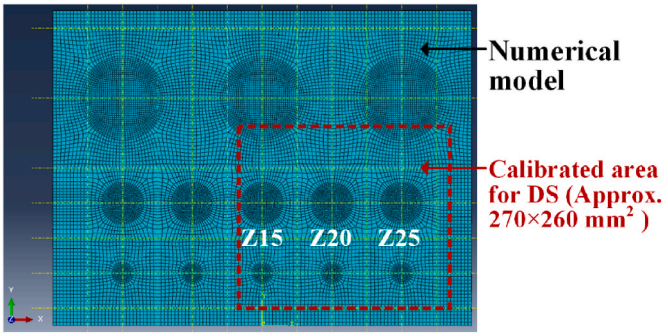

Fig. 7. The established model with mesh. The shear distance calibration area in shearography (DS) experiments marked in dotted red line. (For interpretation of the references to color in this figure legend, the reader is referred to the Web version of this article.)

instrument and averaged axial (through-thickness direction) and radial (in-plane) conductivities of about 0.38 and 0.59 W/(m•°C), respectively, were obtained. These values were included in the model.

As mentioned in Section 2.2, the specimen was heated from the front (defect-free) surface with three halogen lamps (Fig. 2(b)). The heat flux distributions of the three heating scenarios on the specimen surface were experimentally characterised by combining transient temperature measured with an IR camera and a 1D analytical solution of heat conduction in the semi-infinite solid [32,36]. Other methods can also be used to measure energy density [40,41] on the specimen, here the adopted method was used due to its ease of application for constant heat flux heating. The experimentally-estimated heat flux distributions were used as an input of thermal loading in the modelling.

As an ideal mechanical condition, e.g. fully clamped, is quite challenging to achieve in actual experiments due to the significant thickness of the specimen, the test specimen was freestanding on the optical table during the inspection. Therefore the displacement of the bottom surface (along the y-direction) was fixed in the model. The heat loss from the composite laminate to the environment was taken into account in the model. Since the free convection heat transfer coefficient of gas is 2–25 W/(m^2·K) in literature [36] and airflow in the lab is relatively slow, small heat transfer coefficients (front surface of 2–3 W/(m^2·K) and back surface of 8–12 W/(m^2·K)) were selected for the model. The heat loss of the front and back surfaces was set differently due to the remaining heat of the lamps when they were turned off after heating. This approach showed a reasonable accuracy in temperature comparison between the FEM and experiments (Fig. 8 in Section 3.1).

The element type of the model is C3D8RT, a common 3D solid element for coupled temperature-displacement analysis [32,42]. The model consists of about 700000 elements, which takes about 30 h of computational time using a high-performance computing (HPC) cluster. Considering that phase maps are the primary output from the shearography inspections, a MATLAB code was developed to calculate simulated phase maps from the FEM displacement data based on Eq. (2). The experimentally-determined shear calibration according to Ref. [35] was taken into account to correct the simulated phase maps. The shear distance was found to be 8.1 ± 0.32 mm (mean ± std) over the calibrated area. We further compare the simulated phase maps of the calibrated area (Fig. 7) with experimental ones.

3. Results and discussion

This section reports the numerical and experimental results of CST shearography for defect detection of the thick composite laminate with flat bottom holes (Fig. 1(a)). Three heating cases including CST780s, CH780s and CH278s were modelled in Abaqus (FEM) and applied in shearography (DS) experiments. The influence of the three heating scenarios on defect behaviour and defect detection was investigated. In

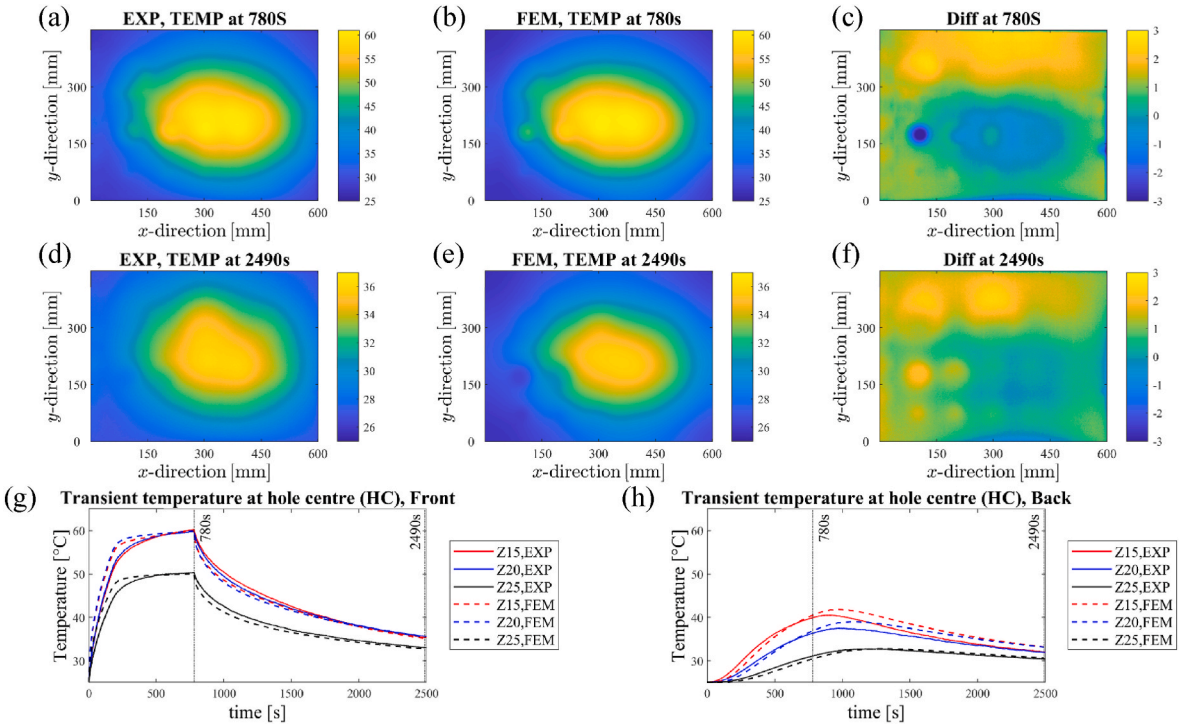

Fig. 8. Model validation for transient temperature: (a)–(c) transient temperature at 780 s (right after heating) measured by experiments (EXP), predicted by FEM and the corresponding difference. (d)–(f) transient temperature at 2490 s (after 1710 s cooling) by EXP, by FEM and the corresponding difference. (g)–(h) transient temperature at the front and the back of the hole centers over time (front measured with the IR camera, back measured with thermocouples).

FEM, both heating and cooling durations were simulated and analysed, while in the shearography experiments, measurements were taken only during cooling because during heating the light from the lamps can saturate the shearography camera sensor. Optical filtering was found to be not efficient enough. As mentioned in Section 2.1, we focus on defects Z15, Z20 and Z25 of diameter 60 mm in this study. The raw data (phase-shifted speckle interferograms) is available at [43] with the metadata to reproduce the experimental results. The unit of phase in shearography is radian, and in this instrument-specimen geometry, 1 rad corresponds to 5.2 με.

3.1. *The validation of the thermal-mechanical model*

As seen from the heating profile in time (Fig. 4), the CST780s heating is the most complicated scenario in this investigation, therefore here we present a comparision of experimental and numerical results of the CST780s heating case for model validation. To validate the model, the temperature and strain behaviours were modelled and measured for a direct comparison.

First, the model validation of temperature behaviour is done. Fig. 8 (a)-8(b) and 8(d)-8(e) shows 2D plots of the transient temperature of the specimen surface by experiment and by FEM at two representative instants of time, namely 780 s (right after heating, the start of shearography measurements) and 2490 s (after 1710 s cooling, the end of shearography measurements), respectively. The difference between measured and predicted temperatures is about ±2 °C (Fig. 8(c) and (f)) when the total range is about 35 °C. It shows a good agreement between experiment and simulation. The difference mainly occurs at the top region. This can be related to the estimated heat flux distribution which is calculated based on 1D heat conduction [32].

Fig. 8(g) and (h) show transient temperature over time at the front and back of the hole centers of defects Z15, Z20 and Z25, respectively. During the first tens of seconds of heating, the temperature from FEM is 2–3 °C higher than that from experiments, this can be because of an overestimated heat flux at the early stage of heating. The maximum temperature difference between the experiment and simulation during cooling is about 2 °C. Possible reasons include a mismatch of estimated heat loss with the actual values during experiments and measurement errors in the conductivity of the through-thickness direction. Based on Fig. 8, the FEM model can predict the transient temperature of the $[0/45/90/-45]_{60}$ GFRP laminate with reasonable accuracy.

Second, the model validation of the simulated phase with the experimental phase (proportional to strain) is given here. The five-step temporal phase shifting method was used to calculate phase maps because of its accuracy. Since phase filtering and phase unwrapping are required to denoise and to remove phase discontinuities, the phase maps were sin/cos filtered with 5 or 6 iterations of circular averaging with a radius of 6 pixels and median filter of an aperture of 5 × 5 pixels respectively. The phase unwrapping was made using the branch-cut method [44]. Fig. 9(a)-9(c) are original phase maps measured with DS, predicted by FEM, and the corresponding difference, respectively. The initial state is right after heating and the final state is after 1710 s cooling (the end of the shearography measurements). The difference between DS and FEM is about −20 to +20 rad for a total phase range of 370 rad. The main contributors are the local fiber-induced deformation (vertical and diagonal lines in Fig. 9(c)), and the top-left and bottom-right corners which may be caused by a difference in the effective boundary conditions and the effectiveness of the shear calibration. A comparison of the original phase along the *a-a* axis is shown in Fig. 9(g), it indicates a good agreement between the experiment and the simulation. It can be noted that experimental data is with variations that appear as lines with angles of 90° and ±45° (e.g., Fig. 9(c) and (g)). The variations are considered to be due to the fiber deformation that is related to fiber layup. While in FEM, the fiber and the resin were homogenised per equivalent layer, hence the phase curve by FEM is smooth.

As no defects are visible in Fig. 9(a) and (b), a compensation process [20,32] was further performed to extract defect-induced phase maps. This process aims to remove global deformation while keeping the defect signal. The defect-induced phase (DIP) maps measured with DS,

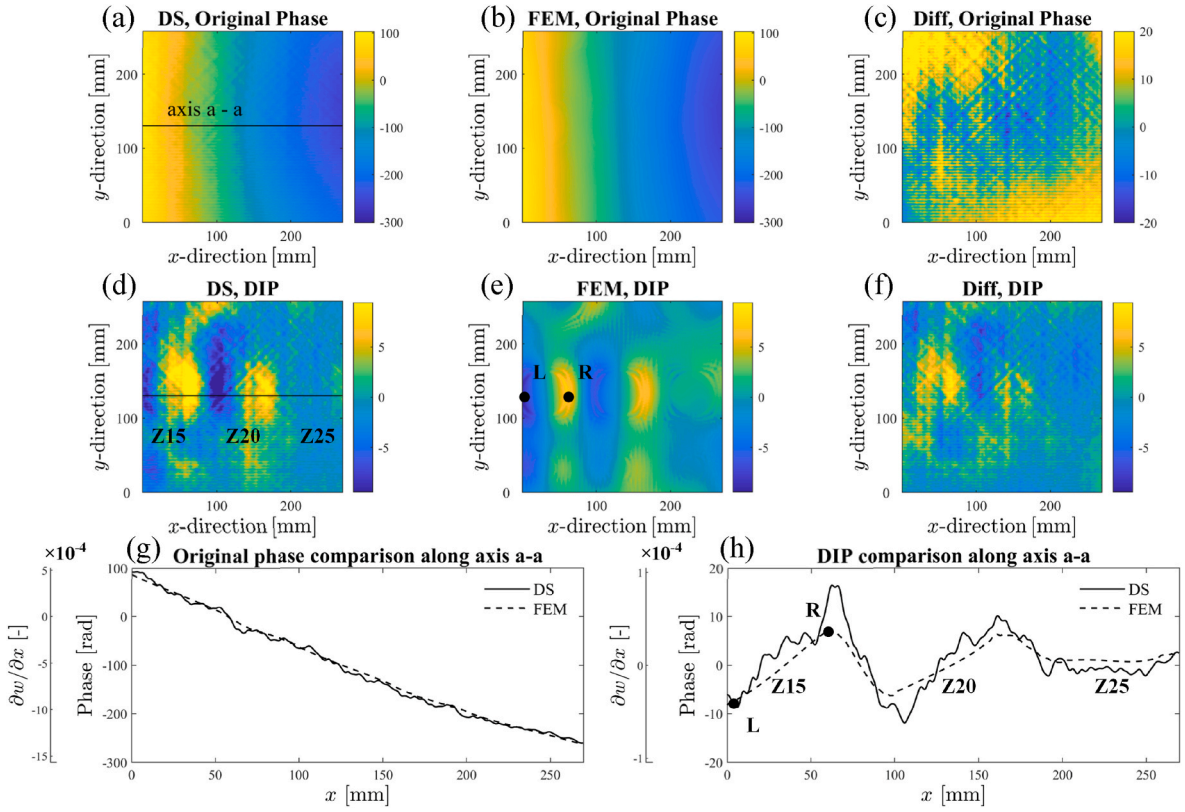

Fig. 9. Model validation for shearography phase: (a)–(c) original phase maps measured with shearography (DS), simulated by FEM and the corresponding difference, respectively. (d)–(f) defect-induced phase (DIP) maps by DS, by FEM and the corresponding difference, respectively. (g)–(h) a comparison of phase along the *a-a* axis for the original phase and defect-induced phase, respectively, (g)–(h) supported with the strain axis. [1 rad corresponds to 5.2 με].

predicted by FEM, and the corresponding difference are shown in Fig. 9 (d)-9(f). The initial and final states were selected to obtain the highest defect signal during cooling. The experimental DIP map and the simulated one show a reasonable agreement; their corresponding difference is about −8 to +8 rad. It can be noted that the total range of the original phase map is about 370 rad. The main contributor to this difference is local fiber-induced deformation. As will be seen later in Fig. 12 in Section 3.2, the standard deviation of fiber-related deformation is about 5 rad. Besides, the temperature mismatch between FEM and experiment during cooling (Fig. 8), the effect of local stiffness (e.g., due to manufacturing defects, Fig. 1(b)), and the errors from the compensation process may also contribute to this difference. From both simulated and experimental DIP maps (Fig. 9(d)-9(e)), the defects Z15 and Z20 are clearly detected, while defect Z25 is close to the detection sensitivity.

Based on both temperature and phase comparisons, the established FEM model can predict the thermal-mechanical response with reasonable accuracy.

3.2. *Analysis of various heating scenarios on defect behaviour and defect detection*

As the thermal-mechanical model is of reasonable accuracy, we combined shearography experiments with the FEM model to obtain a more comprehensive understanding of various heating scenarios on defect behaviour and defect detection in thick composites. This section reports experimental and numerical results to prove the efficacy of the proposed CST heating and the shearography.

First, the temperatures of the three heating scenarios were compared. Fig. 10 shows the transient temperatures at defect depths Z15, Z20 and Z25 (i.e., hole centers at the back surface) for the three heating scenarios.

Both experimental and FEM results show that the maximum temperature at the three defect depths occurs later after the heating stops (e.g., for CST780s, the maximum temperature occurs at around 1100 s while the heating time is 780 s). It indicates a delay between the thermal

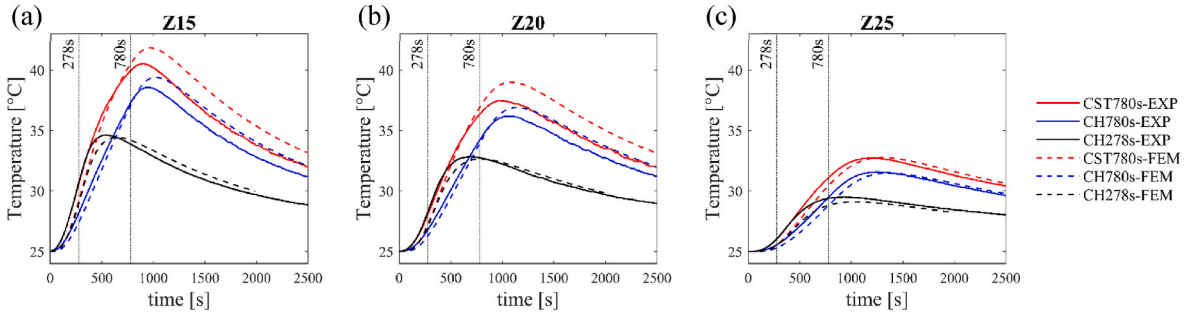

Fig. 10. Transient temperatures at defect depths of (a) 15 mm, (b) 20 mm, and (c) 25 mm for the three heating scenarios. [the solid lines: measured with thermocouples (EXP); the dotted lines: from simulations (FEM)].

excitation and the transient temperature response at the defect region. Moreover, the maximum temperature at those defect depths by CST780s is higher than the other two heating cases; This is straightforward to explain as CST780s uses more energy to excite the object than the other two conventional heating cases. Normally in inspection practice heating energy is not a limiting factor, however, the way the higher energy is applied has to be controlled to ensure safe inspection, which is realised with the proposed CST method.

Second, the shearography phase of the three cases. Fig. 11 shows the comparison of the experimental and simulated DIP maps for the three heatings. As seen from the obtained DIP maps, the defect signal with CST780s (Fig. 11(a) and (d)) is higher than that with CH278s (Fig. 11(c) and (f)) and it is slightly higher than that with CH780s (Fig. 11(b) and (e)).

For defect Z15, the defect signal from CST780s is higher than that from CH780s, while for defect Z20, the defect signals from the CST780s and CH780s heatings are close to each other. This may indicate that although there is a benefit of a higher temperature rise at the various defect depths with CST780s, the influence on defect deformation or defect signal is limited as defect depth increases. As shown in Fig. 11, defects Z15 and Z20 are detectable for the three heating scenarios from both experimental (Fig. 11(a)–(c)) and simulated (Fig. 11(d)-(f)) DIP maps. However, defect Z25 appears to be close to the detection sensitivity for all the three cases.

To further investigate the variation of defect deformation during cooling for the three heating scenarios, the evolution of defect deformation corresponding to the reference state right after heating over the inspection time was made, as shown in Fig. 12(a)-12(c). Signals from the defects at depths of Z15, Z20, and Z25 and the heating scenarios of CST780s, CH780s, and CH278s were obtained by averaging defect-induced phases at the left and right edges of each defect (e.g., (-L + R)/2 in Figs. 9 and 11), as the defect signal is the highest there. Considering that DS measurements were taken only during the cooling of the specimen, here the origin of time was right after heating ($t = 0$ s).

The dotted lines are from the FEM results and the solid lines are from the experimental (DS) results. During the heating ($t = [-780\ 0]$), defect deformation was not available by DS as the light from the lamps can saturate the shearography camera sensor. Therefore it was only derived from FEM data. During the cooling ($t = [0\ 1710]$), defect deformation was derived from both FEM and DS data. In Fig. 12(a), shaded error bars were made for the three heatings in experiments by calculating one standard deviation of the DIPs from a 10 × 200 pixel area (corresponding to 1.6 × 33.0 mm^2 area) at the defect edges. The error sources are expected to mainly come from fiber-related deformation that commonly exists in fiber-reinforced composites under thermal loadings [32]. In Fig. 12(b) and (c), only the shaded error bars of the CST780s case were plotted to make it concise. Fig. 12(d) shows the background deformation of an intact area for the three heating scenarios. The solid (DS) and dotted (FEM) lines were made by averaging the DIPs of an intact region, shaded error regions were also made for the three heatings in experiments by calculating one standard deviation of the DIPs from the intact area. The background deformation mainly comes from complex fiber-related deformation and the compensation process. It can serve as a baseline for defect detection in thick composites.

Table 1 summarises the variation range of DIP during the cooling time for the three defects (data from Fig. 12(a)-12(c)). Both modelling and experimental results show that the DIP range with the CST heating scenario for the defects at 15 and 20 mm depth is higher than with both conventional heatings. The ranges OB and BC (Fig. 12(a)) can both represent the variation range of DIP during the cooling time. In this paper, the range BC was used as the fiber-related noise is lower. The effect of the CST heating decreases as the defect depth increases, while

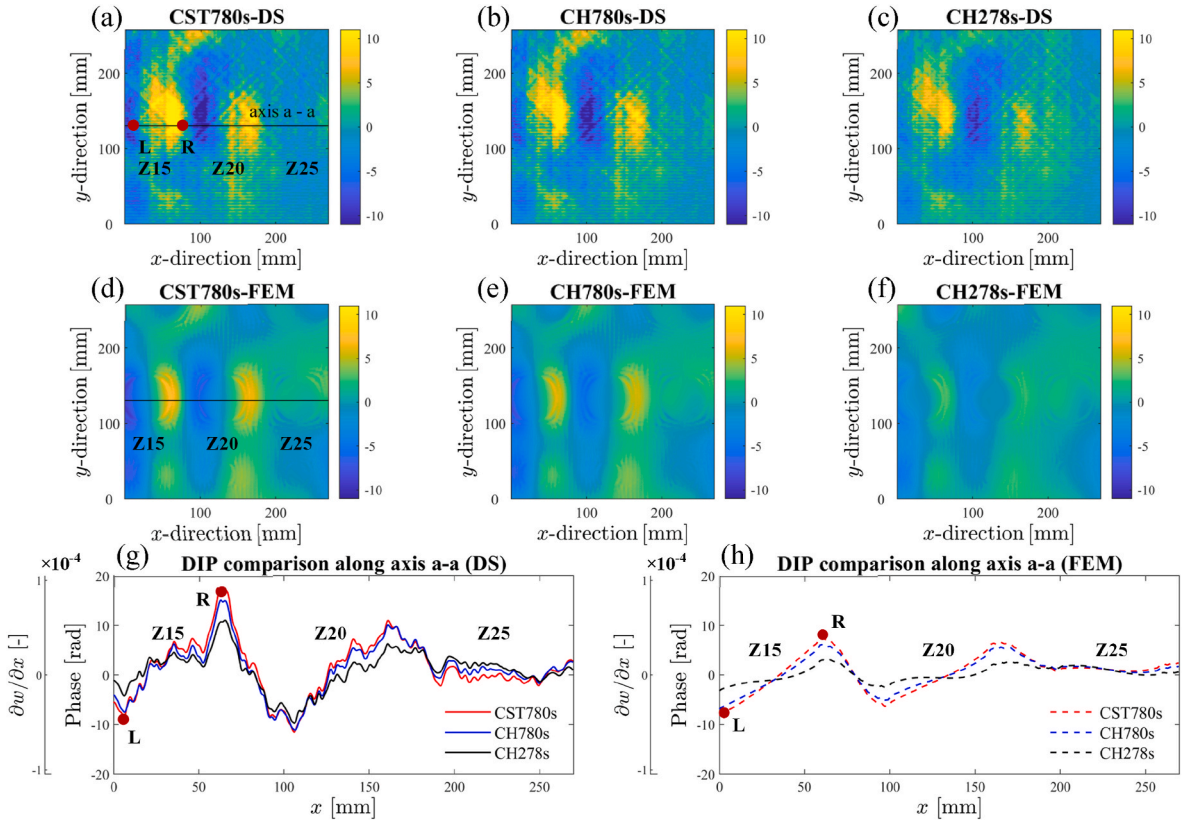

Fig. 11. The defect-induced phase (DIP) maps for the three heating scenarios: (a)–(c) CST780s, CH780s, CH278s from experiments (DS); (d)–(f) CST780s, CH780s, CH278s from simulations (FEM); (g)–(h) the comparison of DIP along the *a-a* axis for the three heating scenarios, supported with the strain axis. The solid lines are from experiments (DS); the dotted lines are from simulations (FEM). [1 rad corresponds to 5.2 με].

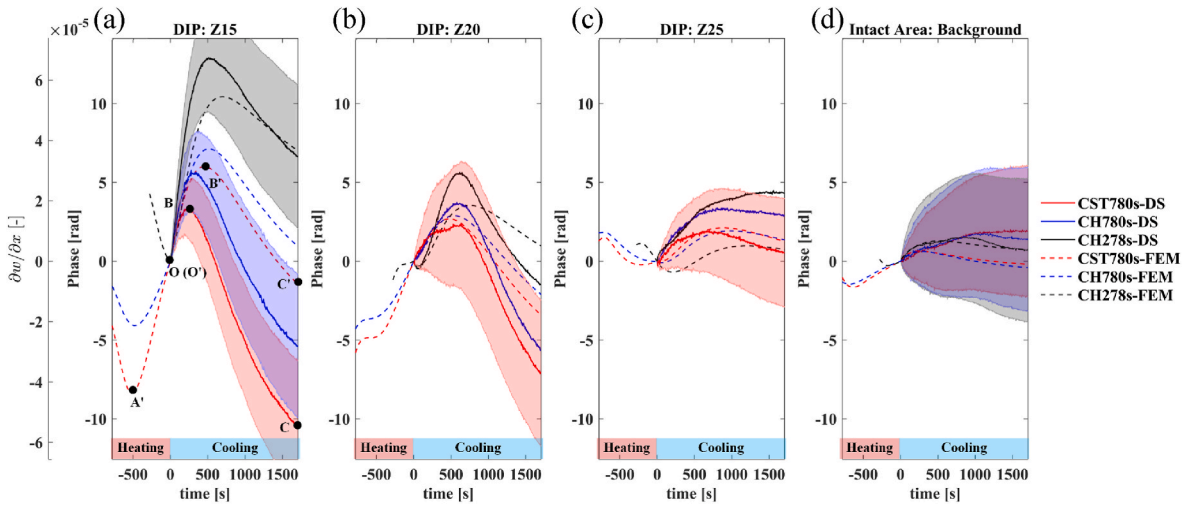

Fig. 12. The defect-induced phases (DIPs) of the three artificial defects over time for the three heating scenarios: (a) Z15, (b) Z20, (c) Z25, (d) background phase of an intact area [the solid lines: from experimental results (DS); the dotted lines: from simulated results (FEM), 1 rad ≈ 5.2 με].

Table 1
Variation range of DIP during the cooling time, phase unit in rad (1 rad ≈ 5.2 με).

	Z15		Z20		Z25	
	FEM	DS	FEM	DS	FEM	DS
CST780s	7.2	13.6	5.7	9.3	0.5	1.3
CH780s	6	10.7	4.9	9	0.3	0.4
CH278s	3	6.3	2.6	7	0.3	0.9

the defect Z25 (Fig. 12(c)) is close to the detection sensitivity as its defect signal is comparable to the fiber deformation from the intact area (Fig. 12(d)). The defect Z25 is rather deep, so more time can be needed for heat to propagate and interact with the defect. From the FEM results, it is seen that during heating the defects Z15 and Z20 have high defect signals (Fig. 12(a)-12(b), up to −8 rad). While the defect Z25 has a rather low defect signal (Fig. 12(c), up to 2 rad), and the signal of the defect Z25 during cooling is also close to the detection sensitivity, which is similar to experimental results. There are two supplementary videos, depending on the reference state, readers can make their own decision on defect Z25.

Fig. 12(a) and (b) also show that there can be an extreme DIP occurring during heating as well as during cooling. For example for the defect Z15, extreme DIP values occur at the time moments of around −500 and 500 s, where only two sets of interferograms need to be taken and further processed (Fig. 13). These time moments provide the highest value of DIP of up to 14.3 rad. Therefore it can be a benefit for implementing an efficient inspection in terms of the inspection duration and the amount of data.

As explained before, we focus on improving deep defect detection with the defect size of 60 mm because of its interest for marine sector. For comparison, the size of realistic defects and damage for marine composites is usually 120 mm and more [45]. Besides, the sensitivity of this shearography technique in terms of minimum detectable defect is around 30 mm in diameter at 15 mm depth with the current heating sources. As the presented results were achieved with the test GFRP panel and in the lab environment, the capability of this technique in presence of real defects and in-situ tests on real marine structures will be investigated in the future.

4. Conclusions

In this work, the novel CST shearography method was proposed and adopted for thick composite inspection. For the first time, defects at 15–25 mm depth have been detected in thick GFRP panel with controlled maximum surface temperature. To the best of our knowledge, no literature has reported on temporally modulated heating that enables the control and selection of maximum surface temperature for thick composite inspection. Moreover, few studies are available on defect behaviour and deep defect detection under various heating scenarios with shearography. This work makes a step forward in safe shearography inspection for deep defect detection where overheating may cause thermal damage. A numerical and experimental study was conducted to analyse defect behaviour and defect detection under three heating scenarios including a new CST heating and two conventional heatings. The

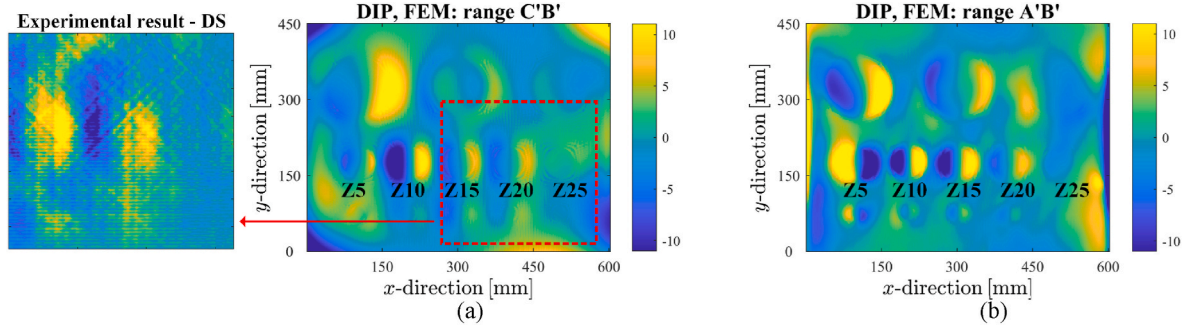

Fig. 13. The DIP maps (for full specimen): (a) choosing reference states during cooling (dotted red area was compared with experiments) and (b) during heating, respectively. The ranges C'B' and A'B' can refer to Fig. 12(a). [Supplementary videos on experimental results are available]. (For interpretation of the references to color in this figure legend, the reader is referred to the Web version of this article.)

main conclusions are summarized as follows:

(1) The advantage of CST heating is that it maximises heating energy input with a controlled and stable maximum surface temperature, along with a higher temperature rise at the defect depth. The experimental and numerical results indicate that defects at 15 and 20 mm depths can be reliably detected with CST heating. The defect-induced phase range with CST heating for these two defects is higher than with both conventional heating methods. For defect Z15, the defect signal with CST780s is about 27% higher than with CH780s and 116% higher than with CH278s. However, the effect of CST decreases as the defect depth increases, with the defect at 25 mm depth close to the detection sensitivity. More time (e.g., a dozen to dozens of minutes of heating) is needed for heat to propagate and interact with defects of 25 mm depth or more.
(2) The established FEM model can serve as a predictive model for investigating and determining the behaviour of the thick composite for defect detection. Real inspection is usually difficult because experiments have problems such as global deformation, non-uniform heating and vibration. Therefore reliable FEM guidance is needed. This FEM guidance saves time during experiments. Besides, FEM during heating shows the benefit of reference states and highlights the value of measurements during heating to be done. The measurements during heating can be done, e.g., by using cyclic heating. The gaps in the heating can allow intermediate speckle interferograms to be recorded without saturating the camera sensor. In addition, laser line-optical filters with narrow transmitted spectral region can be used to isolate the laser light from the wide illumination spectrum.
(3) This study also provides insight for implementing an efficient inspection in terms of the inspection duration and the number of datasets, e.g., only two sets of interferograms during heating and cooling need to be recorded, producing the highest defect-induced phase value for defect detection.

The conclusions were achieved with the test GFRP panel and in the lab environment, the capability of this technique in presence of real defects and in-situ tests on real marine structures will be investigated in the future. Future work will also study the influence of various heating times of CST and amplitudes of the controlled surface temperature on defect detection and characterisation. This work would also apply to the inspection of the structures such as polymeric coatings and paintings where the control of maximum surface temperature is critical.

Author statement

Nan Tao: Methodology, Formal analysis, Software, Investigation, Writing - Original Draft, Visualization. Andrei G. Anisimov: Conceptualization, Software, Supervision, Writing - Review & Editing, Visualization. Roger M. Groves: Supervision, Writing - Review & Editing, Project administration, Funding acquisition.

Declaration of competing interest

The authors declare that they have no known competing financial interests or personal relationships that could have appeared to influence the work reported in this paper.

Data availability

The raw data (phase-shifted speckle interferograms) is available in the 4TU.ResearchData

Acknowledgment

We would like to thank Sian Jones from CITG Faculty, TU Delft for her contribution in performing the conductivity tests. This research was supported by the Operationeel Programma Zuid-Nederland (Op-Zuid) Project as part of the Dutch Composite Maintenance Centre (DCMC), supported by the Europees Fonds voor Regionale Ontwikkeling (EFRO) and the North Brabant province of the Netherlands.

Appendix A. Supplementary data

Supplementary data to this article can be found online at https://doi.org/10.1016/j.ndteint.2023.102907.

References

[1] Greene E. Inspection techniques for marine composite construction and NDE. Rep No SSC-463. Washington, DC: United States Sh Struct Committee; 2012.
[2] Broughton WR. Thick composites. Teddington. 2001.
[3] Hou Y, Li L, Koo JH. Thick-section epoxy composites. In: Chowdhury MA, Armenta JLR, Rahman MM, Asiri A, Inamuddin, editors. Compos. Mater. Rijeka: IntechOpen; 2021.
[4] Tran P, Ghazlan A, Nguyen TP, Gravina R. Experimental and theoretical damage assessment in advanced marine composites. In: Pemberton R, Summerscales J, Graham-Jones J, editors. Mar. Compos. Woodhead Publishing; 2019. p. 55–84.
[5] Groves RM. Inspection and monitoring of composite aircraft structures. In: Beaumont PWR, Zweben CH, editors. Compr. Compos. Mater. II. Oxford: Elsevier; 2018. p. 300–11.
[6] Jerome P. Composite materials in the Airbus A380-from history to future. Beijing Proc. 13th Int. Conf. Compos. Mater. 2001:1–10.
[7] Zhang P. Offshore wind turbines. In: Pemberton R, Summerscales J, Graham-Jones J, editors. Mar. Compos. Woodhead Publishing; 2019. p. 317–44.
[8] García Márquez FP, Peco Chacón AM. A review of non-destructive testing on wind turbines blades. Renew Energy 2020;161:998–1010.
[9] Paboeuf S, de Bruijn A, Evegren F, Krause M, Elenbaas M. A “fast track to approval” process for innovative maritime solutions. In: Okada T, Suzuki K, Kawamura Y, editors. Pract. Des. Ships other float. Struct. Singapore: Springer Singapore; 2021. p. 51–63.
[10] Ibrahim ME. Nondestructive evaluation of thick-section composites and sandwich structures: a review. Composites Part A Appl Sci Manuf 2014;64:36–48.
[11] Nsengiyumva W, Zhong S, Lin J, Zhang Q, Zhong J, Huang Y. Advances, limitations and prospects of nondestructive testing and evaluation of thick composites and sandwich structures: a state-of-the-art review. Compos Struct 2021;256:112951.
[12] Montanini R, Freni F. Non-destructive evaluation of thick glass fiber-reinforced composites by means of optically excited lock-in thermography. Composites Part A Appl Sci Manuf 2012;43:2075–82.
[13] Moradi M, Safizadeh MS. Edge disbond detection of carbon/epoxy repair patch on aluminum using thermography. Compos Sci Technol 2019;179:41–53.
[14] Sinha L, Das D, Nayak AN, Sahu SK. Experimental and numerical study on free vibration characteristics of laminated composite plate with/without cut-out. Compos Struct 2021;256:113051.
[15] Sahu SK, Das P. Experimental and numerical studies on vibration of laminated composite beam with transverse multiple cracks. Mech Syst Signal Process 2020; 135:106398.
[16] Tan KT, Watanabe N, Iwahori Y. X-ray radiography and micro-computed tomography examination of damage characteristics in stitched composites subjected to impact loading. Compos B Eng 2011;42:874–84.
[17] Mehdikhani M, Straumit I, Gorbatikh L, Lomov SV. Detailed characterization of voids in multidirectional carbon fiber/epoxy composite laminates using X-ray micro-computed tomography. Composites Part A Appl Sci Manuf 2019;125: 105532.
[18] Steinchen W, Yang L. Digital shearography: theory and application of digital speckle pattern shearing interferometry, 100. CCH; 2003.
[19] Francis D, Tatam RP, Groves RM. Shearography technology and applications: a review. Meas Sci Technol 2010;21:102001.
[20] Tao N, Anisimov AG, Groves RM. Shearography non-destructive testing of thick GFRP laminates: numerical and experimental study on defect detection with thermal loading. Compos Struct 2022;282:115008.
[21] Hung YY. Shearography for non-destructive evaluation of composite structures. Opt Laser Eng 1996;24:161–82.
[22] Steinchen W, Yang L, Kupfer G, Mäckel P. Non-destructive testing of aerospace composite materials using digital shearography. Proc Inst Mech Eng Part G J Aerosp Eng 1998;212:21–30.
[23] Newman JW. Shearography nondestructive testing of composites. In: Beaumont PWR, Zweben CH, editors. Compr. Compos. Mater. II. Oxford: Elsevier; 2018. p. 270–90.
[24] Krutul EC, Groves RM. Opto-mechanical modelling and experimental approach to the measurement of aerospace materials using shearography and thermal loading. In: Bodermann B, editor. Model. Asp. opt. Metrol. III, 8083. SPIE; 2011. p. 434–42.
[25] Bison PG, Bressan C, Cavaccini G, Ciliberto A, Grinzato EG. NDE of composite materials by thermal method and shearography. In: Wurzbach RN, Burleigh DD,

editors. Thermosense XIX an int. Conf. Therm. Sens. Imaging diagnostic appl, 3056. SPIE; 1997. p. 220–9.
[26] Pfeffer P, Wachter L, Hoffmann D, Bastian M, Schober G. Multiple-flash shearography – a new NDT method for reducing thermal stresses during the inspection process. 10th Int. Symp. NDT Aerosp. 2018:1–8.
[27] de Oliveira BCF, Nienheysen P, Baldo CR, Gonçalves AA, Schmitt RH. Improved impact damage characterisation in CFRP samples using the fusion of optical lock-in thermography and optical square-pulse shearography images. NDT E Int 2020;111:102215.
[28] Gerhard H, Busse G. Lockin-ESPI interferometric imaging for remote non-destructive testing. NDT E Int 2006;39:627–35.
[29] Menner P, Gerhard H, Busse G. Lockin-speckle-interferometry for non-destructive testing. In: Schmit J, Creath K, Towers CE, editors. Interferom. XIV tech. Anal., 7063. SPIE; 2008. 70630C.
[30] Pfeffer P, Wachter L, Hoffmann D, Kolb C, Schober G, Bastian M. A study of multifrequent shearographic lock-In measurements of CFRP. Int. Symp. Struct. Heal. Monit. Nondestruct. Test. 2018:1–7.
[31] Liu L, Guo C, Xiang Y, Tu Y, Wang L, Xuan F-Z. Photothermal radar shearography: a novel transient-based speckle pattern interferometry for depth-tomographic inspection. IEEE Trans Ind Inf 2022;18:4352–60.
[32] Tao N, Anisimov AG, Groves RM. FEM-assisted shearography with spatially modulated heating for non-destructive testing of thick composites with deep defects. Compos Struct 2022;297:115980.
[33] Liu Z, Gao J, Xie H, Wallace P. NDT capability of digital shearography for different materials. Opt Laser Eng 2011;49:1462–9.
[34] De Angelis G, Meo M, Almond DP, Pickering SG, Angioni SL. A new technique to detect defect size and depth in composite structures using digital shearography and unconstrained optimization. NDT E Int 2012;45:91–6.
[35] Anisimov AG, Serikova MG, Groves RM. 3D shape shearography technique for surface strain measurement of free-form objects. Appl Opt 2019;58:498–508.
[36] Bergman TL, Lavine AS, Incropera FP, DeWitt DP. Fundamentals of heat and mass transfer. Wiley; 2017.
[37] Enie RB, Rizzo RR. Three-dimensional laminate moduli. J Compos Mater 1970;4:150–4.
[38] Chan WS, Lin CY, Liang YC, Hwu C. Equivalent thermal expansion coefficients of lumped layer in laminated composites. Compos Sci Technol 2006;66:2402–8.
[39] van Hoorn N, Kassapoglou C, van den Brink WM. Impact Response Prediction and Sensitivity Analysis of Thick Laminated Composite Plates. Techreport NLR-TP-2019-529. 2020.
[40] Krankenhagen R, Worzewski T, Maierhofer C. Cooling-down of thermal thick probes after flash excitation – a measure for the real energy density? Infrared Phys Technol 2015;72:258–65.
[41] Müller JP, Dell'Avvocato G, Krankenhagen R. Assessing overload-induced delaminations in glass fiber reinforced polymers by its geometry and thermal resistance. NDT E Int 2020;116:102309.
[42] Cheng H, Gao J, Kafka OL, Zhang K, Luo B, Liu WK. A micro-scale cutting model for UD CFRP composites with thermo-mechanical coupling. Compos Sci Technol 2017;153:18–31.
[43] Tao N, Anisimov A, Groves R. Shearography data for deep defect detection and characterization in thick GFRP laminates. 4TUResearchData 2022.
[44] Ghiglia DC, Pritt MD. Two-dimensional phase unwrapping: theory, algorithms, and software. Wiley New York; 1998.
[45] Tao N, Anisimov A, Elenbaas M, Groves RM. Shearography non-destructive testing of a composite ship hull section subjected to multiple impacts. Proc. 20th Eur. Conf. Compos. Mater. Compos. Meet Sustain. 2022:469–74.